Contribution of numerical modelling to design oxygen electrode for micro-solid oxide cells: A case study of high-performance nano-columnar La2NiO4 thin films

S. Panisset, A. Riaz, A. Stangl, Mónica Burriel, D. Jauffres

Contribution of numerical modelling to design oxygen electrode for micro-solid oxide cells: a case study of high-performance nano-columnar La_2NiO_4 thin films

S. Panisset[1,2], A. Riaz[1,3], A. Stangl[1], M. Burriel[1], D. Jauffres[2]

1. Univ. Grenoble Alpes, CNRS, Grenoble INP, LMGP, 38000 Grenoble, France

2. Univ. Grenoble Alpes, CNRS, Grenoble INP, SIMAP, 38000 Grenoble, France

3. Univ. Grenoble Alpes, Univ. Savoie Mt Blanc, LEPMI, Grenoble INP, CNRS, 38000 Grenoble, France

Abstract

This article presents a numerical study that aims to guide the development of nano-columnar La_2NiO_4 thin films as high performing oxygen electrodes for micro-Solid Oxide Cell (μSOC). La_2NiO_4 thin films were deposited by Pulsed Injection Metal Organic Chemical Vapor Deposition (PI-MOCVD) and their performance is characterized by Electrochemical Impedance Spectroscopy (EIS) and Electrical Conductivity Relaxation (ECR). Excellent performance is obtained for 1 μm thick film with an Area Specific Resistance (ASR) of 0.12 Ω.cm² at 600°C, making them suitable for low-temperature μSOCs. A Finite Element Method (FEM) model has been implemented and used to predict the ASR and impedance spectra in order to guide further optimization of the film thickness and morphology. After experimental validation of the model using various electrode thicknesses, the optimal value is estimated to be between 3 to 4 μm for the temperature range of 450-650°C. For each temperature and thickness, the model can clearly predict whether the electrode is limited by the surface exchange reactions or the bulk diffusion. The simulations revealed that the gas diffusion process is not rate-limiting when the electrode

thickness is below 5 µm and the temperature is below 650°C. Furthermore, a geometrical parameters analysis study allowed to determine the ideal nano-columnar morphology for this promising electrode composition.

Key words: Oxygen electrode, lanthanum nickelate, reversible solid oxide cells (rSOCs), finite element modelling, thin film solid oxide cells (TF-SOCs), electrochemical impedance spectroscopy (EIS)

1. Introduction

In recent years, the interest in Solid Oxide Cells (SOCs) has surged, owing to their unrivalled efficiency for both the generation of clean electricity from green hydrogen when working as Solid Oxide Fuel Cell (SOFC), and for the production of green hydrogen from renewable resources when working as Solid Oxide Electrolysis Cell (SOEC). However, the oxygen electrode, also known as the air electrode, poses a significant challenge in this technology when working at intermediate to low temperatures. This is primarily due to its thermally activated processes with high activation energies, which are responsible for the highest polarization resistance contribution of the complete cell. To overcome this obstacle and at the same time reduce the operating temperature to a lower range (< 600°C) to avoid long-term degradation of the cells, a promising solution is the design of electrodes based on engineered nanostructures [1], [2]. This compelling proposition has stimulated the development of micro–solid oxide fuel cells (µSOFCs), also called thin-film solid oxide fuel cells (TF-SOFCs), wherein conventional SOCs have been downscaled to dimensions below one micron, while retaining a considerable surface area [3]–[5]. These ground-breaking advancements in µSOFCs open up new and more sustainable ways for powering electronic portable devices, and for other potential applications such as offshore electrical energy storage or transportation.

However, despite the enthusiasm surrounding µSOFCs, several challenges have still to be overcome to increase their power output and ensure long-term stability, particularly regarding the nanostructured electrodes. Concerning the oxygen electrode performance itself, *Yang et al.* highlights that the electrode activity is a combination of the intrinsic activity, characterized by the material physicochemical properties, and the apparent

activity, defined by the number of active sites [6]. This apparent activity is crucial in Mixed Ionic Electronic Conductor (MIEC) thin film electrodes, where the active reaction region is the whole electrode surface, including the surface provided by open porosity. Therefore, designing and optimizing the optimal electrode 3D architecture and morphology are of great importance to enhance the performance of μSOCs.

In response to the necessity for optimizing electrode architectures and film microstructures, numerous analytical and numerical models have been implemented [7]–[12]. These models are versatile tools to study the impact of microstructural parameters such as the porosity, the tortuosity, the specific surface area, the electrode thickness *etc.* The Adler-Lane-Steele (ALS) model is one of the first 1D analytical models that has been widely used in SOFC development [11]. The ALS model assumes a macro-homogeneous morphology, and an analytical expression can be derived for thin film electrodes, where the surface exchange reactions dominate the bulk diffusion. This model for finite-length electrodes is constructed under the hypothesis that the electrode thickness L is at least 3 times lower than the penetration length l_δ, which corresponds to the electrode electrochemically active thickness. The model relates the area-specific resistance (ASR) to the microstructural parameters for a MIEC thin film electrode [7], [13]. However, obtaining quantitative specific surface area values (exposed surface area over volume) at such a small scale is a significant challenge and required very peculiar techniques such as titration [14]. Additionally, the ALS model does not take into account inhomogeneous morphology, and even for thin film electrodes, the hypothesis $3L < l_\delta$ is not always fulfilled. The use of analytical modelling based on strong hypotheses can lead to inaccurate modelling of thin film electrodes and mislead their optimization for better performance.

The first member of the Ruddlesden-Popper lanthanum nickelate phases, $La_2NiO_{4+\delta}$ (L2NO4), has been extensively studied for SOFC and SOEC oxygen electrode and oxygen permeation membranes, due to its fast ionic diffusivity, good electrical conductivity, and remarkable catalytic activity towards the oxygen reduction reaction (ORR), with low activation energy and high chemical stability [15]–[19]. In our group, L2NO4 electrodes with nano-columnar morphology were recently deposited by Pulsed Injection Metal Organic Chemical Vapor Deposition (PI-MOCVD) leading to a significant enhancement of the oxygen exchange activity [20].

In the present study, we choose a combined numerical and experimental approach to better understand the role of the microstructure and guide further improvement of thin film oxygen electrodes for µSOCs. A 3-dimensional (3D) finite element method (FEM) model is used to predict the ASR and the impedance spectra of nano-architectured MIEC electrodes. Using this approach, we can effectively evaluate the optimal film thickness and design for this type of electrodes, saving valuable time that would otherwise be lost in experimental trial-and-error methods.

The model is implemented using COMSOL Multiphysics™ software. It requires geometrical parameters of the film morphology, as well as intrinsic material properties such as over-stoichiometric oxygen δ, oxygen concentration at equilibrium $c_{O^{2-}_{eq}}$, surface exchange coefficient k_{chem}, diffusion coefficient D_{chem}, and external parameters such as temperature, oxygen partial pressure, and external potential. The 3D FEM model can be solved in either stationary or dynamic mode to obtain the ASR or the impedance spectra, respectively. Electrochemical impedance spectroscopy (EIS) and Electrical Conductivity Relaxation (ECR) measurements have been performed to assess the electrode polarization resistance and the electrochemical activity for various film thicknesses to calibrate and validate the model. The application of the 3D model provides interesting guidelines to enhance low temperature µSOC performance by increasing the apparent activity of the oxygen electrode.

2. Experiment methods

2.1 Thin Film Growth

$La_2NiO_{4+\delta}$ (L2NO4) thin films were grown using Pulsed Injection Metal Organic Chemical Vapor Deposition (PI-MOCVD) on 10 x 10 mm² double side polished Yttria-Stabilized Zirconia (YSZ) (100 oriented) single crystals (Crystec Gmbh). The precursor solution was prepared by dissolving $La(TMHD)_3$ and $Ni(TMHD)_2$ (TMHD = 2,2,6,6-tetramethylheptane-3,5-dionate), both from Strem Chemicals, in m-xylene (1,3-dimethylbenzene) from Alfa Aesar. The concentration of the solution was 0.02 mol/L with a La/Ni ratio of 4.5. This ratio has been optimized as compared to our previous work where it was 5 [20]. The evaporation process took place in several stages

between 220 °C and 280 °C and the deposition temperature was 650 °C. The injection frequency and opening times were set at 1 Hz and 2 ms, respectively. The carrier gas concentration was 34% Ar and 66% O_2 and the total pressure inside the reactor was kept at 5 Torr. The thickness of the films was controlled by the number of pulses injected and varied between 200 and 1000 nm. The injection frequency was increased to 4 Hz for the deposition of the thicker film to reduce the deposition time. No morphological or structural changes were detected between the films deposited at 1Hz and 4Hz (see Fig. S1).

2.2 Structural Characterization

The structural analysis and phase identification of the films was done using X-ray diffraction (XRD; Brucker D8 Advanced Diffractometer) in θ-2θ geometry using a Cu-Kα source (λ = 0.154 nm). The XRD spectra were corrected using the substrate peak positions as reference. The surface morphology was observed using FEG Gemini SEM 500 microscope in secondary and backscattered electron modes with an acceleration voltage of 3 kV. The microstructure images were treated and analysed using IPSDK Explorer software (Reactiv'IP).

2.3 Functional Characterization

The polarization resistance of the L2NO4 electrodes (10 x 10 mm²) was measured using EIS in a home-built setup with tubular furnace and connected to a Biologic SP200 potentiostat. Current collection layer was made by sputtering approximately 10 nm layer of Au on top of the L2NO4 films and then brush painting Au over a surface of 8 x 8 mm². Measurements were carried out on symmetrical and asymmetrical cells in dry air between 450 to 650 °C. For asymmetrical cells, a porous Ag layer is painted on the back of the YSZ, serving as a current collector and relatively low impedance counter-electrode. Data was collected between 100 kHz and 100 mHz using an AC voltage of 50 mV.

The EIS results were complemented by ECR measurements at low temperature. The electrical conductivity is measured in the Van-der-Pauw configuration using a small excitation current of 1µA. Four electrical probes are mechanically pinned onto Ag electrodes painted in the corner of a 5 x 5 mm² sample. The temperature and the

pO_2 are controlled in a high temperature cell (Nextron) and continuously recorded together with the conductivity using LabVIEW. The atmosphere is kept at 1 atm and a constant flow rate of 1000 mL/min was employed. The oxygen partial pressure is controlled by the mixture of highly pure O to N flows. The evolution of the conductivity is measured as a function of consecutive abrupt steps in pO_2 between 210 and 10 mbar in the temperature range between 300 and 400 °C (see Fig. S2).

3. Model description

The chosen approach is a 3D FEM model, where the nano-columnar film microstructure is simplified and reconstructed from SEM observations. Similar models implemented for thick electrodes can be found in the literature applied to $La_{0.58}Sr_{0.4}Co_{0.2}Fe_{0.8}O_{3-\delta}$ material [12], [21], [22] and 60:40 $La_{0.6}Sr_{0.4}Co_{0.2}Fe_{0.8}O_{3-\delta}$-$Ce_{0.9}Gd_{0.1}O_{2-\delta}$ composites [9] and successfully show the influence of microstructural parameters, such as porosity, tortuosity, and specific surface area, on the electrode performance.

3.1 Physics

Numerous theoretical and experimental studies have been devoted to examining the electrochemical mechanisms of MIEC electrodes, with particular emphasis on the LSCF material [11], [23]–[25], as one of the most promising compositions for intermediate temperature SOFC operation. Electrochemical models for over-stoichiometric materials such as L2NO4 are rare, nevertheless Sdanghi *et al.* demonstrated that, under Open Circuit Potential (OCP) and for porous thick electrode, the reaction mechanism for L2NO4 is controlled by the bulk path below 650°C and by the surface path at higher temperatures [26].

Based on this knowledge, the present model implements the bulk path, where the oxygen is incorporated at the gas/electrode interface, in opposition of the surface path characterized by a direct charge transfer at the Triple Phase Boundary (TPB). The model considers the four physicochemical processes commonly considered in other models [9], [12], [13], [21], [22], namely: i) the gas diffusion in the film porosity, ii) the oxygen surface exchange between the gas phase and the electrode material, iii) the bulk diffusion of the oxygen ions, and iv) the charge

transfer at the electrode/electrolyte interface. The dissociative adsorption, reduction, and incorporation of oxygen into the bulk at the surface of the electrode are all comprised in the global chemical exchange coefficient k_{chem} that combines all steps. The oxygen ion transport in the bulk is described by the chemical diffusion coefficient D_{chem}.

The total pressure in the pore phase is assumed uniform, so that the convection transport is neglected. Instead, the mass transport is solely governed by local partial pressure gradients. The diffusion of oxygen molecules in pore channels to the electrochemically active surface of the oxygen electrode is computed using the dusty-gas-model [27] described as:

$$\frac{\partial x_{O_2}(\vec{x},t)}{\partial t} + \nabla\left(-\frac{p}{RT}\left[\frac{1-(1-\sqrt{M_{O_2}/M_{\mathrm{N}_2}})\cdot x_{O_2}(\vec{x},t)}{D_{O_2N_2}} + \frac{1}{D_K(d_p)}\right]^{-1}\cdot \nabla x_{O_2}(\vec{x},t)\right) = 0 \qquad (1)$$

where x_{O_2} is the oxygen gas molar fraction. The binary diffusion coefficient $D_{O_2N_2}$ is given by:

$$D_{O_2N_2} = 1.86\cdot 10^{-3}\cdot T^{\frac{3}{2}}\frac{\sqrt{M_{O_2}^{-1}+M_{N_2}^{-1}}}{p\cdot\Omega\cdot\sigma_{O_2N_2}} \qquad (2)$$

The gas phase is depicted as a binary mixture of oxygen and nitrogen. The binary diffusion coefficient is defined by Chapman-Enskog and includes the oxygen and nitrogen molar masses, M_{O_2} and M_{N_2}, the total gas-phase pressure p, the collision integral Ω, and the collision diameter $\sigma_{O_2N_2}$ [28]. The Knudsen diffusion coefficient D_K describes the interaction of oxygen molecules with the pore walls. Therefore, it depends on the geometry and more specifically in this case, on the size of the gap between two nano-columns denoted as d_p:

$$D_K = \frac{2}{3}d_p\cdot\sqrt{\frac{8RT}{\pi M_{O_2}}} \qquad (3)$$

where R is the ideal gas constant and T is the temperature. The oxygen gas diffusion can, under specific conditions, result in a x_{O_2} – or oxygen partial pressure p_{O_2} – gradient in the columns gap.

The surface exchange at the gas/electrode interface is driven by the deviation of the ionic concentration $c_{O^{2-}}$ from the equilibrium concentration $c_{O^{2-}_{eq}}$, reached in open circuit conditions, via an applied potential difference.

$$\overrightarrow{J_O} \cdot \vec{n} = k_{chem}\left(c_{O^{2-}_{eq}} - c_{O^{2-}}\right) \tag{4}$$

where $\overrightarrow{J_O}$ is the flux density of oxygen ions in $mol.m^{-2}s^{-1}$. The relatively high electronic conductivity implies that the influence of the electron transport in the electrode is negligible compared to other potential rate-determining steps. Therefore, the model assumes that electrons are instantly available at the electrode surface and ensure then the local electroneutrality in the material.

Due to the assumption stated above (constant electric field), the driving force of the ionic bulk diffusion results only from the concentration gradient. Thus, the transport of oxygen ions is described by Fick's second law:

$$\frac{\partial c_{O^{2-}}(\vec{x},t)}{\partial t} - D_{chem}\left(T, p_{O_2}\right) \cdot \nabla c_{O^{2-}}(\vec{x},t) = 0 \tag{5}$$

The oxygen ion concentration at the equilibrium $c_{O^{2-}_{eq}}$ depends on the temperature and the atmospheric oxygen partial pressure p_{O_2} and is given by:

$$c_{O^{2-}_{eq}}\left(T, p_{O_2}\right) = C_1(T) \cdot \log(p_{O_2}) + C_2(T) \tag{6}$$

The values of the temperature dependent parameters $C_1(T)$ and $C_2(T)$ are obtained by fitting the over-stoichiometric oxygen δ values from [29] and the molar volume V_m from [30] using the two following relations:

$$c_{O_i^{2-}} = \frac{\delta}{V_m} \tag{7}$$

$$c_{O^{2-}_{eq}} = \frac{4+\delta}{\delta} c_{O_i^{2-}} \tag{8}$$

where $c_{O_i^{2-}}$ is the interstitial oxygen concentration. The oxygen ions are exchanged at the electrode/electrolyte interface. The local charge transfer overpotential η_{CT} is given by:

$$\eta_{CT} = U_{\mathcal{N},interface}\left(p^{elec}_{O_2,interface}, p_{O_2,CE}\right) - \left(\phi_{elec} - \phi|_{z=l_{ely}}\right) \quad (9)$$

$$U_{\mathcal{N},interface} = \frac{RT}{2F} \cdot ln\sqrt{\frac{p^{elec}_{O_2,interface}}{p_{O_2,CE}}} \quad (10)$$

where $U_{\mathcal{N},interface}$ is the Nernst's potential between the electrode/electrolyte interface and the counter electrode (CE), ϕ_{elec} and $\phi|_{z=l_{ely}}$ are the potential in the electrode and at the electrolyte interface, respectively. The oxygen partial pressure in the electrode $p^{elec}_{O_2}$ is calculated from the equation (6) knowing the local oxygen ion concentration $c_{O^{2-}}$. A local oxygen ion exchange current density J_{CT} can be determined at the electrode/electrolyte interface through a charge transfer resistance ASR_{CT} that will be fixed to $0.1\ m\Omega.cm^2$ [8].

$$J_{CT} = \frac{\eta_{CT}}{ASR_{CT}} \quad (11)$$

Then, the boundary condition at the interface between the electrode and the electrolyte is set as:

$$\overrightarrow{J_O} \cdot \vec{n} = \frac{J_{CT}}{2F} \quad (12)$$

where F is the Faraday constant. In the electrolyte, the ionic current density $\overrightarrow{J_{ion}}$ conservation applies:

$$\nabla.\overrightarrow{J_{ion}} = 0 \quad (13)$$

where $\overrightarrow{J_{ion}}$ is determined by the electrical field $\vec{E}$ derived from the gradient of the electrical potential ϕ :

$$\overrightarrow{J_{ion}} = \sigma_{ely}(T).\vec{E} + \frac{\partial \vec{D}}{\partial t} \quad (14)$$

$$\vec{D} = \varepsilon_0 \varepsilon_r \vec{E} \quad (15)$$

$$\vec{E} = -\nabla\phi \quad (16)$$

$\vec{D}$ is the electric displacement field, ε_0 the vacuum permittivity and ε_r the dielectric constant. The electrolyte is described as a conductive media with a temperature dependent effective conductivity $\sigma_{ely}(T)$. At the electrode/electrolyte interface, the following boundary condition applies:

$$\overrightarrow{J_{ion}}.\vec{n} = -J_{CT} \quad (17)$$

Finally, the electrode performance is measured thanks to the electrode ASR (ASR_{elec}). This parameter is determined by subtracting the electrolyte ASR contribution (ASR_{ely}) to the global ASR of the model (ASR_{model}):

$$ASR_{elec} = ASR_{model} - ASR_{ely} = \frac{\eta_{model}}{I} - \frac{l_{ely}}{\sigma_{ely}} \quad (18)$$

where η_{model} is the total voltage loss of the model and fixed at 50 mV, I is the surface integral of the current density at the electrode/electrolyte interface, l_{ely} is the thickness of the electrolyte.

3.2 Impedance spectra

To implement the calculation of the electrode impedance spectra, the model is solved in time-dependent domain over the range of frequencies 100 kHz to 5mHz. As shown in Fig. S3, the input voltage is a sinusoidal function, which will induce a sinusoidal excitation of the half-cell. 12 periods are simulated to reach sufficient number of periods in the stationary regime. The current curve is extracted from the Comsol simulation and fitted by a sinusoidal function ($A * sin(\omega t - \varphi)$) using a Matlab script. The amplitude A and the phase shift φ are used to calculate the real and imaginary parts of the electrode impedance Z by:

$$Re(Z) = \frac{U_0}{A} * \cos(\varphi) \quad (19)$$

$$Im(Z) = \frac{U_0}{A} * \sin(\varphi) \quad (20)$$

where U_0 is the amplitude of the imposed voltage excitation η_{model}, fixed to 0.05 V.

4. Results and discussion

4.1 Thin film characterization

Structural characterization

The crystal structure of the film was characterized by X-ray diffraction in the θ–2θ configuration as in Fig. 1 a) shown for a representative 500 nm thin film grown on YSZ. The diffraction pattern obtained is in good agreement with the reported La_2NiO_4 structure (space group I4/mmm, ICDD reference 04-015-2147). A polycrystalline growth with (110), (020), and (103) preferential orientations is observed. Very small additional peaks can be observed suggesting the presence of minor traces of La_2O_3 oxide (ICDD reference 01-074-5408), probably due to a small excess of La in the film. This very small amount of impurities is expected to have a negligible effect on the electrode's overall performance.

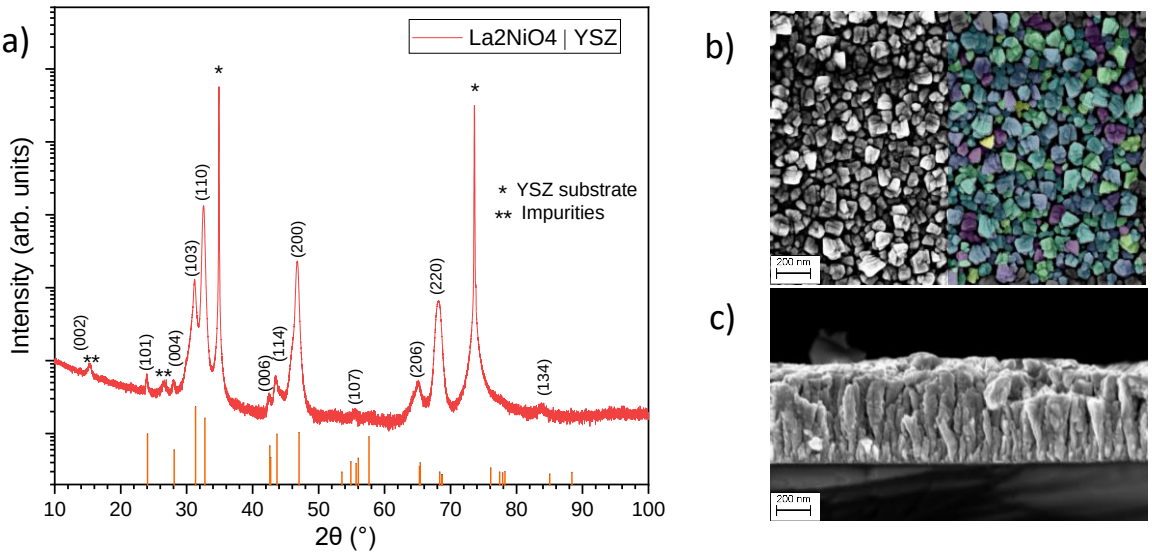

Fig. 1: a) XRD diffraction pattern of a 500 nm nano-columnar La_2NiO_4 electrode showing (110), (020), and (103) preferential orientations; b) SEM in top view of a 200 nm thick L2NO4 film showing the irregular nano-column shape and the labelling of each nano-column (coloured right side) used for image quantitative size analysis, and c) SEM cross-section view of a 500 nm thick L2NO4 film depicting the nano-columnar growth of the film.

Microstructural characterization

The microstructure is characterized by SEM top and cross-section view as shown in Fig. 1 b) and c), respectively. The porous film is formed by nano-columns similar to the ones reported in [20]. By SEM images post-treatment analysis, the size of the top surface of each grain was measured, giving an averaged column size of 56 nm assuming a brick geometry. A rather large size distribution (± 28 nm) has been measured, indicating a competitive

growth between columns. A thin dense layer is observed on top of the YSZ electrolyte, at the base of the L2NO4 film. Its thickness is assessed to be around 40 nm from SEM cross-section and previous Transmision Electronic Microscope (TEM) observations performed by *Stangl et al.* [20]. The gaps between the columns are estimated to be 8 ± 2 nm wide.

4.2 Model geometry

Microstructural parameters play a crucial role on the electrode performance and have been extensively studied in a large diversity of models [8], [10], [31]–[35]. Homogenized models, such as the Adler-Lane-Steel model [11], represent the microstructure in terms of macrohomogeneous parameters as porosity, volume-specific surface area and tortuosity. Other models involve simplified microstructures such as spheres, cubes [12] or rods [36]. More complex microstructural models have been recently developed and are based on the reconstruction of the real microstructure by FIB-SEM [37]–[39] or X-ray tomography [40].

As shown Fig. 1 b), the size of the microstructural features of the film used in this work (columns, pore channels, *etc.*) are of the order of magnitude of the resolution limit of conventional FIB-SEM. For this reason, the model geometry is simplified and based on SEM and TEM image analysis. This geometry is depicted as a juxtaposition of nano-columns standing on a thin dense layer deposited on top of the electrolyte surface (see Fig. 2 a)). All the geometrical parameters of the model geometry are summarized in Table 1. The electrolyte thickness is fixed to 100 nm as it has no impact (see Equation (18)) on the electrode ASR calculation when taken sufficiently large.

Only one quarter of a nano-column is modelled to save computation time. As shown in Fig. 2 b), the complete nano-column is reconstructed by YZ- and XZ-planar symmetry. A mesh convergence study has been performed to ensure that the mesh used is fine enough.

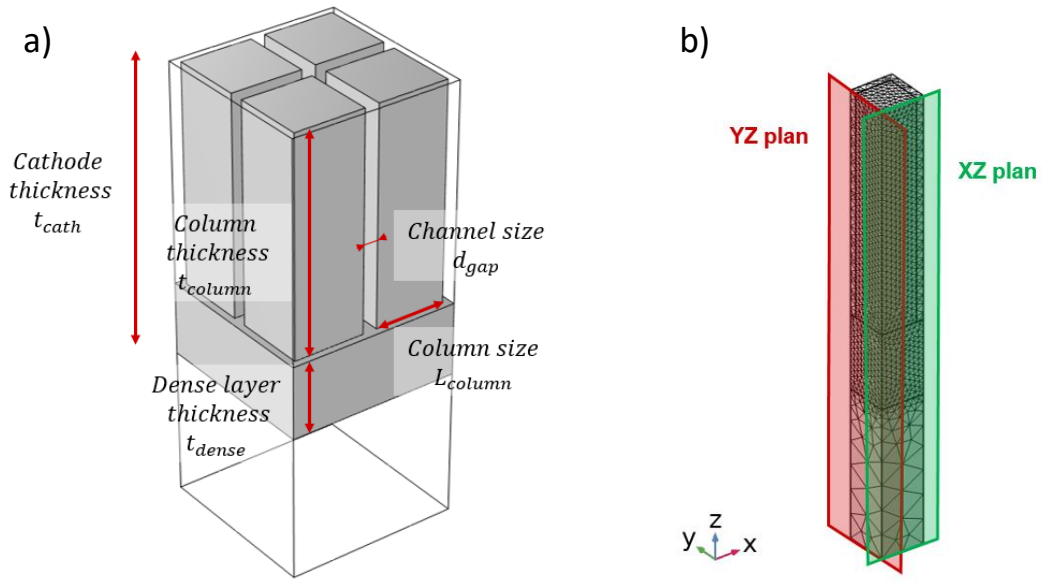

Fig. 2: a) Representation of four nano-columns showing the geometrical parameters; b) representation of the mesh of one quarter of a nano-column with its two planar symmetries.

Table 1: Geometrical parameters used as an averaged nano-column geometry and range of values tested in the parametrical study.

Geometrical parameters	Symbols	Values	Range of values tested	
Cathode thickness	t_{cath}	200 nm	[0.1; 10] µm	Measured
Electrolyte thickness	t_{ely}	100 nm	-	Fixed
Nano-column size (length and width)	L_{column}	56 nm	[4; 100] nm	Measured
Gap between nano-column size	d_{gap}	8 nm	[0.2; 20] nm	Measured
Electrode dense layer thickness	t_{dense}	40 nm	[2; 199] nm	Measured

4.3 **Chemical surface exchange coefficient (k_{chem})** determination

The 3D model developed allows to study the effect of the thin film morphology on the electrode performance aiming to provide a quantitative prediction able to assess the optimal electrode thickness. Recently, Stangl *et al.* showed that the electrode ASR of a nanoporous thin film of L2NO4 decreases when the thickness increases [20]. The authors explained that the nano-columnar growth of the film allow to create more exposed surface and thus

more active sites are available for surface exchange reactions. However, as the thickness increases, the performance improvement may be limited by the ionic diffusion in the electrode material and/or the gas diffusion inside the pore channels. In their article, Stangl *et al.* also highlight that the slope of k_{chem} measured from thin dense and porous film are different, which suggests that the surface termination or surface chemistry of the two film morphologies could differ, as well as the absence/presence of highly active nano-features such as kinks and edges [20].

For this reason, here the chemical surface exchange coefficient k_{chem} was experimentally measured by EIS and the ALS model applied using the thin electrode hypothesis ($3L < l_d$). The 200 nm film is assumed to be thin enough, and the diffusion coefficient does not affect the ASR value. In such conditions, the ALS model for a half-symmetrical cell is given by the following equation [13]:

$$Z_{chem} = \frac{RT}{4F^2}\frac{\gamma_O}{aLk_{chem}c_{mc}(1 + i\omega t_{chem})} \tag{21}$$

where R is the ideal gas constant, T the temperature, F the Faraday's constant, $\gamma_O = \pm\frac{1}{2}\frac{\partial\, lnp_{O_2}}{\partial\, lnc_O}$ the thermodynamic factor, a the specific surface area, L the electrode thickness, k_{chem} the chemical exchange surface coefficient, c_{mc} the oxygen concentration in the crystal lattice and t_{chem} is the time constant. The specific surface area, $a = S/V_{tot}$, is the total electrode surface in contact with the gas, divided by the total volume.

By rearranging the equation (21) and taking $ASR = Re(\mathrm{Z_{chem}})$, k_{chem} is given by:

$$k_{chem} = \frac{RT}{4F^2}\frac{\gamma_O}{aL \cdot \mathrm{ASR} \cdot c_{mc}} \tag{22}$$

where a is calculated from the model geometry and is equal to $4.88\ 10^7 m^{-1}$. All other material parameters implemented in the model are summarized in Table 2 and come from the literature. The k_{chem} coefficients calculated from the measured ASR values were found to be equal to $2.02 \cdot 10^{-6}$, $5.89 \cdot 10^{-7}$, and $1.53 \cdot 10^{-7}$ $\mathrm{m/s}$ at 600, 550 and 500°C, respectively. These values were fitted to an Arrhenius law ($E_a = 1.50\ eV$) to

be used in the model. The values are in good agreement with the data reported in the literature for L2NO4 thin films [20], [41], even though k_{chem} values vary considerably across different sources in the literature (Fig. 3 a)). As highlighted in the recent study by Ascolani-Yael *et al.* [42], in addition to differences in sample morphology, sources of discrepancies originate in particular from the use of three different methods for measuring kinetic parameters, each with its own set of advantages and disadvantages: ECR – electrical conductivity relaxation [15], [20], [41], [43], EIS – electrochemical impedance spectroscopy analysis [41], [44], and IEDP/SIMS – isotope exchange depth profiling combined with secondary ion mass-spectrometry [45]–[49].

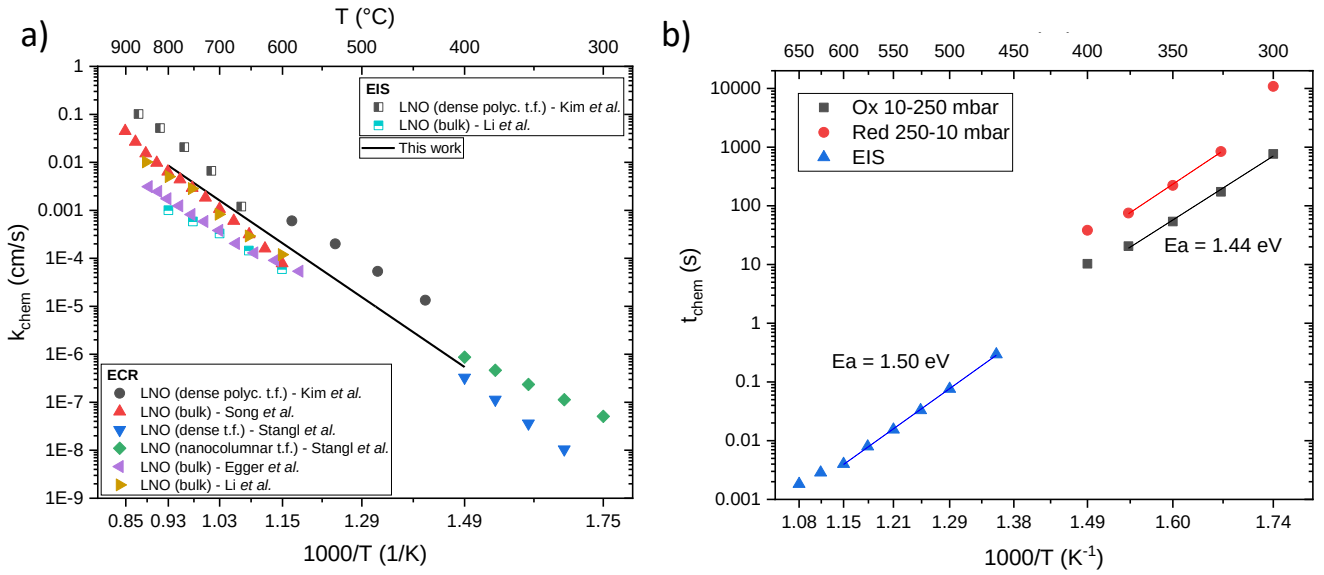

Fig. 3: a) Compilation of chemical surface exchange coefficient k_{chem} (cm/s) reported in the literature for L2NO4 thin films and dense pellets [15], [20], [41], [43], [50], [51]. *Surface exchange coefficients obtain using EIS methods have been corrected by the L2NO4 thermodynamic factor from* [15]*; b) Comparison of characteristic time constants t_{chem} of a 200 nm nano-columnar thin film obtained by EIS and ECR. ECR measurement has been performed in both reduction (Red) and oxidation (Ox) from oxygen partial pressure of 250 to 10 mbar and inversely.*

The characteristic time constant t_{chem} obtained by fitting EIS results with a RQ equivalent circuit (using $t_{chem} = \frac{1}{\omega_{max}}$), has been compared with the ECR experiment at lower temperatures. Fig. 3 b) demonstrates that both methods yield comparable results within their respective temperature ranges, as evidenced by the alignment of the sets of data in the Arrhenius plot. This confirms the results from Kim et al. that shows similar alignment in there k_{chem} coefficients from ECR and EIS measurements on dense polycrystalline thin film [41]. The higher the

characteristic time constant for the reduction step can be attributed to the lower final oxygen partial pressure ($p_{O_2}^{final}$). As exemplified in Fig. S4, the t_{chem} value isn't determined by the nature of the oxygen exchange (reduction/oxidation), but rather by the $p_{O_2}^{final}$. In EIS, the oxygen partial pressure in the MIEC electrode is slightly oscillating around 210 mbar, which is rather close to the gas phase condition of the ECR oxidation step shown in Fig. 3 b). The ECR method is therefore suitable to determine the k_{chem} coefficient as, in the case of surface-controlled processes, k_{chem} and t_{chem} are related by the following equation:

$$k_{chem} = \frac{1}{at_{chem}} \tag{23}$$

Table 2: YSZ and L2NO4 material parameters implemented in the model.

	Material parameters	Symbol	Value at each temperature			Units	Reference
			500 °C	550 °C	600 °C		
YSZ	Electrical conductivity	σ_{ely}	8.26e-2	1.69e-1	3.18e-1	S/m	[52]
	Dielectric constant	ε_r	10	10	10	-	[12]
L2NO4	Oxygen chemical diffusion L2NO4	D_{chem}	2.53e-11	8.75e-11	2.63e-10	m^2/s	[26]
	Oxygen concentration at equilibrium	$c_{O_{eq}^{2-}}$	70614	70369	70147	mol/m^3	[26]
	Oxygen overstochiometry	δ	0.110	0.106	0.100	-	[26]
	Thermodynamic factor	γ_O	376	380	384	-	[15]

4.4 Model validation and optimal thickness

Experimental EIS measurements were performed at OCV and at various temperature and electrode thicknesses to validate the model. The experimental results were fitted by an equivalent circuit using a Constant Phase Element (CPE) in parallel with a resistance (R1-R2/CPE). The Area Specific Resistance (ASR – in $\Omega \cdot cm^2$) is calculated from electrode polarization resistance and the sample in plane area.

Experimental results (Fig. 4) show that the electrode performance is improved significantly when the electrode thickness increases. The ASR obtained at 600°C (under air and OCV for the 200 nm, 540 nm, and 1000 nm films

are 0.56, 0.23, and 0.12 $\Omega.cm^2$, respectively. The latest value is, to our knowledge, the lowest ASR value reported in the literature for L2NO4. Vibhu *et al.* reported a polarization resistance of 0.93 $\Omega.cm^2$ – under the same conditions – using a 20 µm thick and porous L2NO4 electrode deposited on GDC/8YSZ by Screen Printing (SP) [53]. Sharma *et al.* measured a polarization resistance of 3.33 $\Omega.cm^2$ for a thick (35 µm) and porous electrode deposited by Electrochemical Spray Deposition (ESD) on a CGO electrolyte [19]. Further improvement of the R_{pol} was obtained with their architectured double-layer ESD + SP electrode reaching 0.42 $\Omega.cm^2$ at 600°C [19].

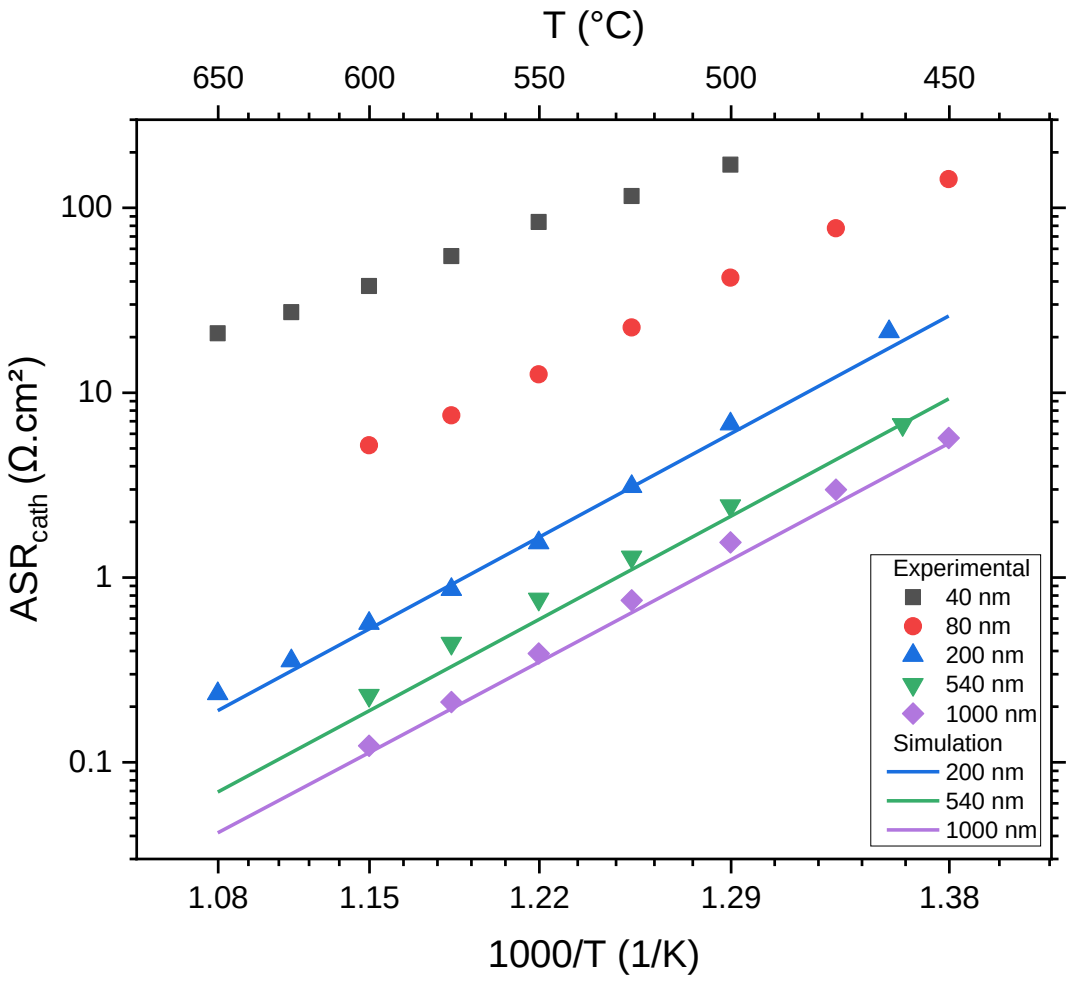

Fig. 4: Comparison of measured and simulated L2NO4 ASR_{cath} for the dense (40 and 80 nm) and nano-columnar (200, 540 and 1000 nm) L2NO4 electrode as a function temperature (dots = experimental, line = simulation). All other model geometrical parameters are fixed.

Simulations have been performed using the k_{chem} value (based on the Arrhenius law) derived from EIS measurements on a 200 nm film, to predict the ASR values for the 200, 540, and 1000 nm thick thin films. Fig. 4 shows the good match between the experimental and numerical results, confirming that model geometry remains valid when the film thickness increases from 200 nm to 1 µm for a temperature range between 400 and 650 °C. Both results confirm that the ASR decreases when the electrode thickness increases. Indeed, the columnar growth results in a significant increase of the surface available for oxygen incorporation into the L2NO4 electrode. Thus, within the thickness range discussed so far, the thicker the electrode, the better the performance. The simulation shows a linear variation between the ASR and the electrode thickness. From the 200 nm thin film, the ASR is reduced by a factor 2.7 and 5 for a 540 nm and 1000 nm film, respectively. Given that the specific surface area of the model column remains relatively stable across different column thicknesses, this observation is consistent with the Equation (21) established for surface exchange limited case. However, this is true only if the microstructure is similar for all the thin films. In addition, the surface exchange limitation is only valid for the case of very thin films, and, as will be shown later, the appearance of other regimes (bulk or gas diffusion limited) whit increasing film thickness implies that an optimal electrode thickness exists, where the ASR has a minimum.

To find the optimal electrode thickness, a parametric study on the electrode geometrical characteristics was carried out. The model mesh was adapted accordingly. The variation of the ASR as a function of the thickness shown in Fig. 5 clearly displays two distinct regions. For low thicknesses, the electrode performance increases with electrode thickness, showing a surface exchange reaction limitation. For thicker films, the ASR does not vary with the electrode thickness, which indicates that the bulk diffusion process is limiting. The two dotted lines represent the ALS analytical model in the thin and semi-infinite length hypotheses. The graph validates that the 200 nm electrode is only limited by the surface exchange, validating the initial hypothesis employed in utilizing the ALS equation for thin electrodes. Within the co-limited region, only the FEM model is able to predict accurately the ASR values for each temperature and microstructure. The simulation suggests that the optimal electrode thickness is approximately 3 µm at 650 °C and above 4 µm at 450 °C. It can be noted that the optimal

thickness increases slightly when the temperature decreases due to the difference in activation energy between the k_{chem} (-1.50 eV) and D_{chem} (-1.38 eV) coefficients. In other words, the penetration length of the L2NO4 electrode increases with decreasing temperature. When comparing to our best 1 µm thick film, depositing a 3 or 4 µm film would results in a relatively modest ASR decrease. Thus, this raises the question of whether it is worth to multiply the electrode thickness by 3 or 4, and consequently the volume of the solution injected, for a performance improvement around 1.5 times.

Upon closer examination of Fig. 5 at higher temperatures (650 °C), it can be seen that the ASR increases slightly for thick electrodes (above 5000 nm). This increase has been associated to the gas diffusion mechanism. Indeed, as the ORRs is faster at higher temperature, the gas diffusion starts limiting the oxygen gas molecule influx at the electrode surface.

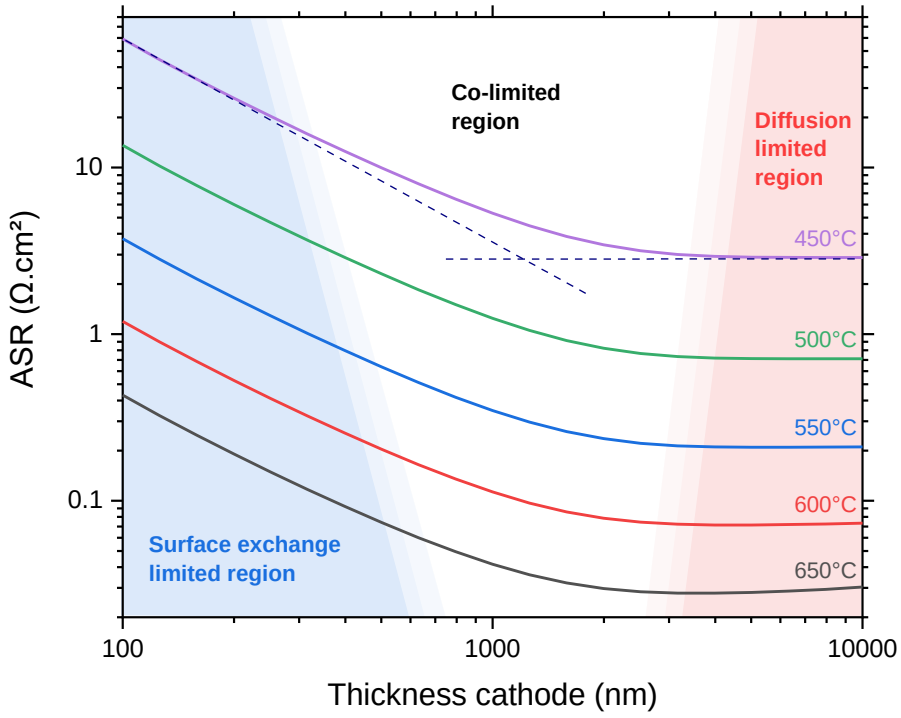

Fig. 5: Electrode ASR variation with the electrode thickness for various temperatures showing the surface exchange limited region at lower electrode thicknesses, the diffusion limited region for thicker electrode, and the co-limited region. The two dotted lines represent the ALS analytical model in the thin and semi-infinite length hypotheses. Gas diffusion limitation is visible at 650 °C for high electrode thicknesses.

4.5 Electrochemical impedance spectra

The 3D FEM model can be solved in dynamic mode to simulate the impedance spectra of an ideal L2NO4 nano-column. The frequency range used is from 100 kHz to 5 mHz, and the AC amplitude voltage is 50 mV. Fig. 6 a) shows the simulated impedance spectra of a 1 µm L2NO4 nano-columnar film in the temperature range of 500 °C to 600 °C. The simulation shows a gradual change of the Gerischer-type semi-circle shape, and the total impedance reduction with increasing temperature. The Gerischer impedance shape is characterized by a 45° slope at the high frequency range of the semi-circle.

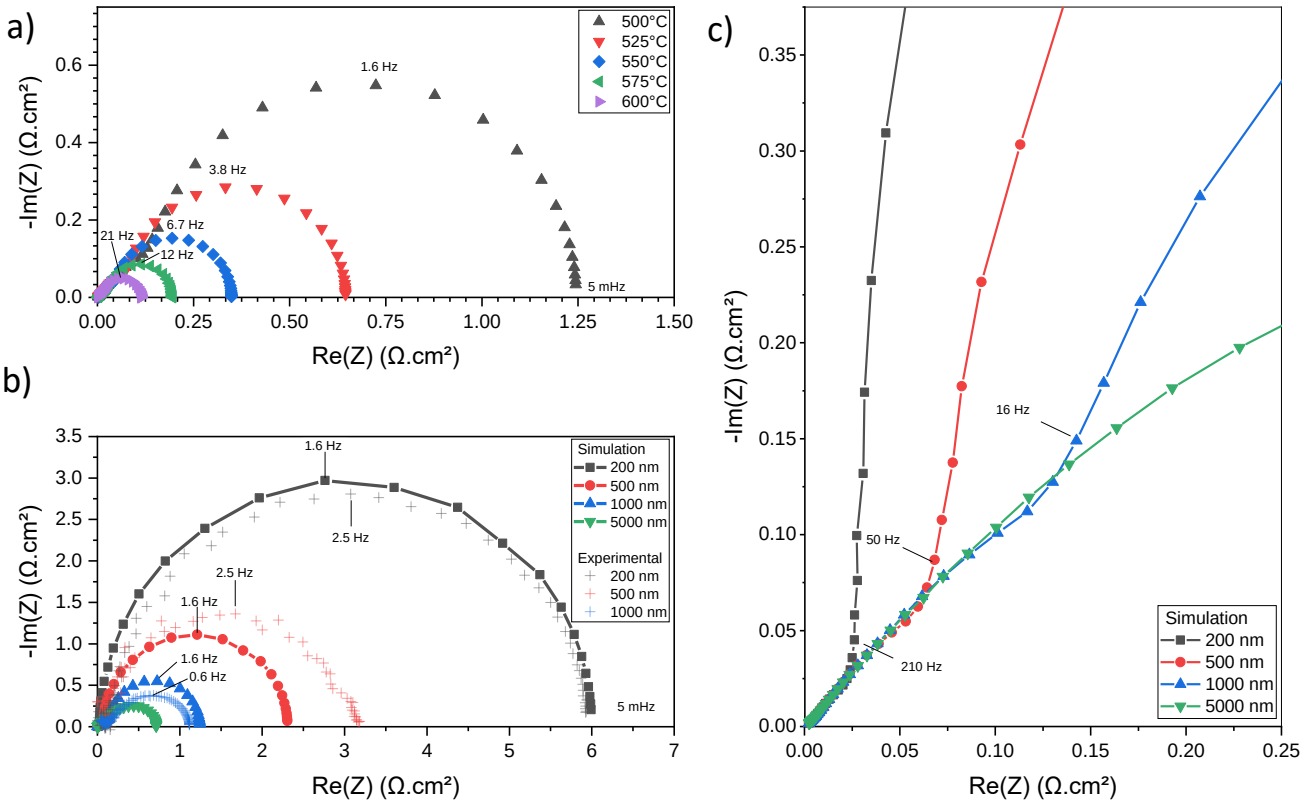

Fig. 6: a) Simulated impedance spectra for a 1 µm L2NO4 nano-columnar electrode at various temperatures showing the reduction of Gerischer-type impedance with increasing temperature; b) Experimental and simulated impedance spectra at 500 °C for various thickness of a L2NO4 nano-columnar electrode; c) Magnification on the high frequency region of the simulated curves.

Fig. 6 b) shows the comparison between the simulated and the experimental impedance spectra. The series resistance, commonly attributed to the ohmic resistance of the YSZ electrolyte, has been subtracted from the

experimental spectra. As shown in the Arrhenius plot of ASR_{series} in Fig. S5, the activation energy of the series resistance of these three films are close to 1 eV and their absolute values match with YSZ single crystals measurements from the literature [54] and from our own experiments. As expected, the impedance spectrum is very similar in the case of the 200 nm film used to assess k_{chem}. For the 500 nm and 1000 nm, the semi-circles are flattened and the Re(Z) value are slightly different, which can be explained as the model does not consider the inhomogeneities of the electrode material or the frequency-dependent processes that might lead to a n exponent ≠ 1 (in the equivalent circuit using Constant-Phase Element, CPE). It should be noted that the purpose of the 3D FEM model (in AC mode) is not to fit the EIS curves obtained experimentally as the equivalent electrical circuit fitting is good enough to extract the ASR, C, R_{series} and n. The simulated impedance spectra are used instead as prediction of the Nyquist plot, and thus, to achieve a better understanding of the limiting mechanisms that occur. As exemplified in Fig. 6 a) and c), the simulated spectra clearly show a transition from a perfect semi-circle at lower temperature and lower electrode thickness to a pure Gerischer impedance at higher temperature and higher electrode thickness.

To investigate the potential limitation of oxygen gas diffusion process at high temperatures and for thicker electrodes suspected in Fig. 5 for the curve at 650°C, the impedance spectra of a 5 µm thick film with 2 nm pore channels and decreasing oxygen partial pressure to enhance limitation by gas diffusion process were simulated. Fig. 7 shows that the reduction of oxygen partial pressure leads to a significant increase of the impedance at low frequencies. The ASR is more than doubled from 2.1 10^{-1} to 5 10^{-3} atm, and multiplied by a factor of 3.9 when the oxygen partial pressure dropped to 1 10^{-3} atm. The Distribution of Relaxation Times (DRT) method was employed to distinguish between the contributions of oxygen gas diffusion and ionic bulk diffusion more effectively. This method converted the impedance data from the frequency domain into a distribution function of relaxation times [55]. This method does not depend on the equivalent circuit chosen to fit the spectra. Fig. 7 b) shows that, except for the spectra at 0.21 atm, two peaks (or two-time constants) can be distinguished. The peak between 10 and 100 Hz would correspond to the oxygen gas diffusion and the second one close to 1 kHz

would be related to the oxygen surface exchange kinetics & bulk diffusion of O^{2-} [56]. It is worth noting that gas limitation in this case cannot be identified without a close examination of the spectra and the use of DRT.

The simulated results shown in Fig. 6 and Fig. 7 are obtained at OCV, however, it is important to mention that lower (higher) ASR values are expected for La_2NiO_4 electrodes under anodic (cathodic) polarization [57], [58]. As the model is implemented using Nernst equation assuming thermodynamic equilibrium, the polarization conditions (anodic or cathodic) cannot be directly applied, which is a current limitation of the model. The effect of the electrode polarization is outside the scope of this study, but interested readers may wish to consider other models based on 1D elementary kinetics that can be found in the literature [58]–[60]. It should also be noted that we assumed constant k_{chem} and D_{chem} coefficients along the whole nano-column thickness, which is only valid for negligible pO_2 gradients within the pore channels. In the case of gas diffusion limitation (thick electrode, high temperatures, or low pO_2), because of pO_2 gradient, the simulated performance would be slightly overestimated, as k_{chem} and D_{chem} should slightly decrease with pO_2 (see Fig. S4).

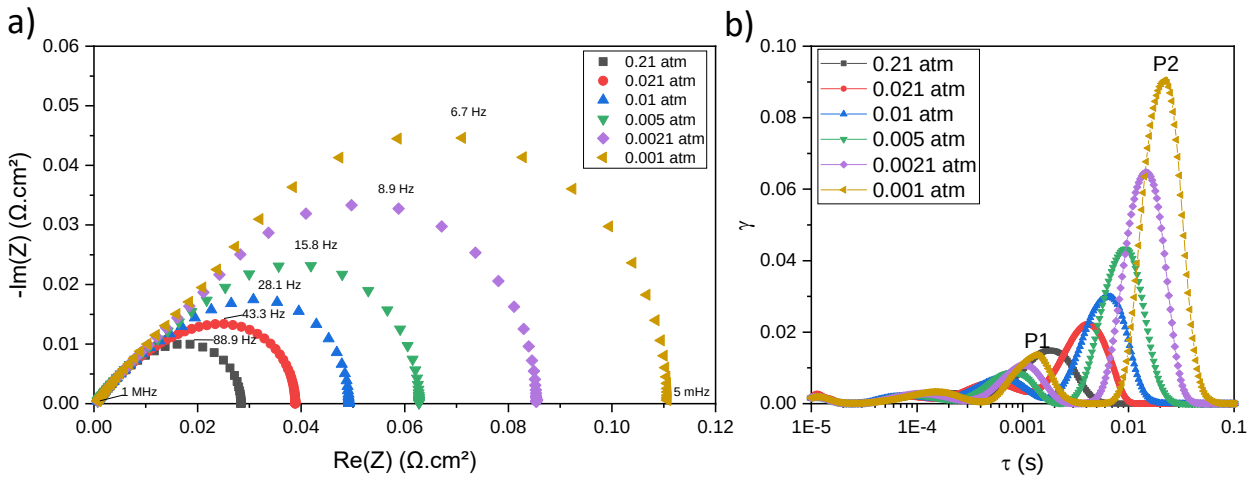

Fig. 7: a) Simulated impedance spectra of 5 µm nano-columnar electrode (with 2 nm pore channels) at various oxygen partial pressures at 650°C; b) Distribution of relaxation times analysis.

In the temperature range of 450 to 650°C, the model reveals an optimal electrode thickness around 3 to 4 µm. Thus, above this thickness limit, the ASR is either constant when the cell is operating at low temperature, or it increases as the gas diffusion becomes limiting at high temperature. Nevertheless, this optimal electrode

thickness assumes that there is no change of the film morphology. For instance, the dense layer thickness, the grain size and the pore size between columns can be tuned by changing the deposition parameters. This underscores the need to study the impact of the film morphology on the electrode performance, shown in the next section.

4.6 Geometrical parametric study

In the previous sections, the electrode thickness was increased only by varying the column height. Along with the column height, three other geometrical parameters were studied here: the dense layer thickness, the grain size (the width of the column), and the gap size (space between two columns). All these geometric parameters are illustrated Fig. 2 a). The model is solved in stationary mode using parametric studies to investigate the influence of all the geometric parameters, and the results are summarized in Fig. 8 a), b), and c) for the dense layer thickness, the gap size, and the column size, respectively. The first parametric study shows that the increase of the dense layer is detrimental for the electrode performance as it results in a surface reduction and thus a reduction of active sites for oxygen incorporation. However, an extremely thin dense layer or its total suppression might not be desirable as it could imply current constriction in the electrode or in the electrolyte near the interface. In addition, it can impact the electron conduction, particularly when columns are isolated without connectivity to the current collector, resulting in the inability to transfer electrons between columns.

The gap size significantly affects the ASR and exhibits an optimum value, that depends on the temperature and on the oxygen partial pressure pO_2 in the atmosphere. The sharp ASR increase at lower gap size is due to the Knudsen diffusion that results in a non-negligeable pO_2 gradient inside the very narrow channels between the columns. This causes a gas diffusion limitation. Then, at higher gap sizes, the gas diffusion is not the limiting process anymore. When increasing the gap size, the specific surface area decreases, which results in an increase of the ASR following equation (21). The optimal gap size value increases for higher working temperature and lower pO_2 as the pO_2 gradient in the pore channels becomes non-negligible, and thus, the gas diffusion becomes the limiting mechanism. This effect is shown by the dotted line for lower oxygen partial pressure. For this

simulation, the k_{chem} coefficient has been adapted according to the lower pO_2 based on the experimental results Fig. 3 a) and Fig. S4 a).

Finally, the same analysis can be done with the variation of column size. The specific surface area increases with the column size except below 8 nm, which corresponds to the gap size. Below the gap size, the specific surface area decreases with the column size. As expected, the ASR follows the evolution of the specific surface with the column size.

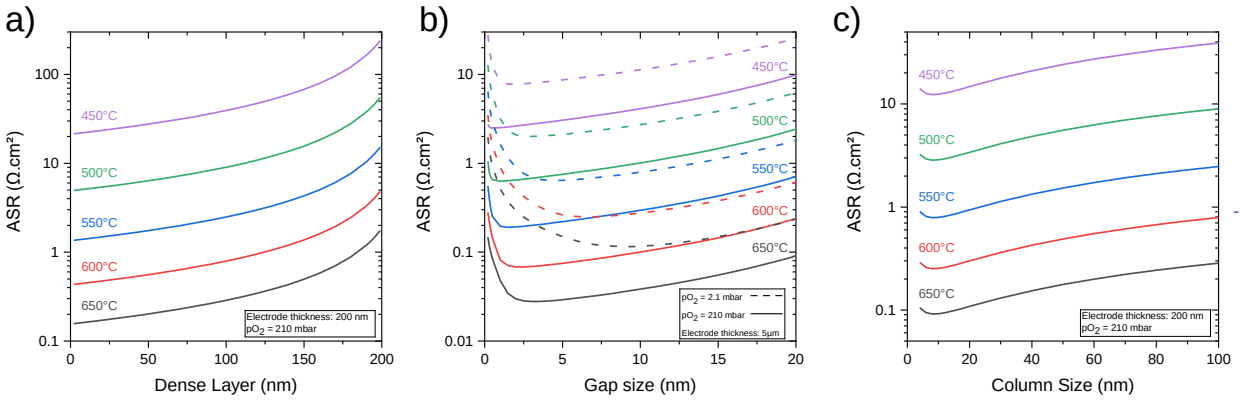

Fig. 8: ASR variation by varying the a) dense layer thickness, b) gap sizes between two columns, and c) column sizes for a temperature range of 450-650°C. The oxygen partial pressure and electrode thickness are fixed to 0.21 bar and 200 nm, respectively, except for the gap size parameter, where the electrode thickness is fixed to 5 µm.

In short, the parametric studies highlight that the dense layer must remain thin compared to the column thickness. The optimal nano-columnar architecture is a relatively porous and compact film with very thin and elongated nano-columns (high aspect ratio). However, too thin pore channels might be detrimental at high temperature and/or under high polarization due to the gas diffusion limitation for thick films and high surface exchange activity, that might lead to depletion of gaseous oxygen. These results show a theoretical architecture optimisation and provide valuable guidelines for linking experimentally obtained microstructures to electrode performance.

5. Conclusions

In conclusion, this work presents a versatile numerical tool, a 3D FEM model, for investigating the performance of thin film oxygen electrodes in µSOCs. The model provides a comprehensive description of the nano-architecture of the electrode and incorporates the oxygen transport mechanisms, including gas diffusion, surface exchange reactions, bulk diffusion, and charge transfer at the electrode/electrolyte interface. The experimental work conducted in this study focused on $La_2NiO_{4+\delta}$ nano-columnar thin film deposited using pulsed-injection metal-organic chemical vapor deposition (PI-MOCVD). The experimental ASR values measured at low temperatures are very low (ASR = 0.12 $\Omega.cm^2$ at 600°C) for the 1 µm L2NO4 thin electrode. The model was carefully calibrated and validated using experimental EIS and ECR results, demonstrating a good match across various electrode thicknesses.

The key findings of the model shed light on the optimization of nano-columnar electrode morphology. The optimal electrode thickness was determined to be in the range of 3 to 4 µm for a temperature range of 650 to 450°C. In addition, the ideal nano-columnar morphology was characterized by highly elongated and closely spaced columns. Importantly, the model shows that no gas diffusion limitation was observed below 5 µm in the given model geometry.

This numerical model holds promising prospects for further exploration. It can be extended to investigate the performance of other materials, deposition techniques and electrode architectures, such as different film morphologies or composite materials. By leveraging the insights gained from this study, researchers can continue to refine and optimize µSOFC electrode designs, ultimately advancing the development of efficient and practical micro solid oxide fuel cells.

Author Contributions

Investigation: AS, AR, SP; formal analysis: SP; methodology: SP, DJ, MB; conceptualization: SP, DJ, MB; writing – original draft: SP; writing – review & editing: SP, DJ, MB, AS.

Acknowledgements

This work was funded by the European Union's Horizon 2020 research and innovation program under grant agreements no. 824072 (Harvestore project) and no. 101017709 (EPISTORE) and by the Centre of Excellence of Multifunctional Architectured Materials "CEMAM" n° ANR-10-LABX-44-01 as part of the "Investments for the Future" Program. This research has benefited from characterization equipment of the Grenoble INP - CMTC platform.

Data Availability Statement

The data that support the findings of this study are openly available in Zenodo at https://zenodo.org/records/8319001, reference number 8319001.

Conflicts of interest

There are no conflicts to declare.

References

[1] K. Develos-Bagarinao, Ed., *Nanoengineered Materials for Solid Oxide Cells*. IOP Publishing, 2023. doi: 10.1088/978-0-7503-4064-9.

[2] M. Acosta, F. Baiutti, A. Tarancón, and J. L. MacManus-Driscoll, “Nanostructured Materials and Interfaces for Advanced Ionic Electronic Conducting Oxides,” *Adv Mater Interfaces*, vol. 6, no. 15, Aug. 2019, doi: 10.1002/admi.201900462.

[3] A. Evans, A. Bieberle-Hütter, J. L. M. Rupp, and L. J. Gauckler, “Review on microfabricated micro-solid oxide fuel cell membranes,” *Journal of Power Sources*, vol. 194, no. 1. pp. 119–129, Oct. 20, 2009. doi: 10.1016/j.jpowsour.2009.03.048.

[4] F. Chiabrera, I. Garbayo, N. Alayo, and A. Tarancón, “Micro solid oxide fuel cells: a new generation of micro-power sources for portable applications,” in *Smart Sensors, Actuators, and MEMS VIII*, SPIE, Jun. 2017, p. 102460S. doi: 10.1117/12.2269454.

[5] J. Zhang, S. Ricote, P. V. Hendriksen, and Y. Chen, “Advanced Materials for Thin-Film Solid Oxide Fuel Cells: Recent Progress and Challenges in Boosting the Device Performance at Low Temperatures,” *Adv Funct Mater*, p. 2111205, Mar. 2022, doi: 10.1002/adfm.202111205.

[6] G. Yang *et al.*, “Toward Reducing the Operation Temperature of Solid Oxide Fuel Cells: Our Past 15 Years of Efforts in Cathode Development,” 2020, doi: 10.1021/acs.energyfuels.0c01887.

[7] S. Panisset, M. Burriel, J. Laurencin, and D. Jauffres, “Modelling of solid oxide cell oxygen electrodes,” *Journal of Physics: Energy*, vol. 5, no. 2, p. 022003, Apr. 2023, doi: 10.1088/2515-7655/ACC5B1.

[8] B. Rüger, A. Weber, and E. Ivers-Tiffée, “3D-modeling and performance evaluation of mixed conducting (MIEC) cathodes,” *Electrochemical Society*, vol. 7, no. 1, pp. 2067–2074, 2007.

[9] O. Celikbilek, D. Jauffres, L. Dessemond, M. Burriel, C. L. Martin, and E. Djurado, “A Coupled Experimental/Numerical Approach for Tuning High-Performing SOFC-Cathode,” *ECS Trans*, vol. 72, no. 7, pp. 81–92, Apr. 2016, doi: 10.1149/07207.0081ecst.

[10] J. E. Mortensen, M. Søgaard, and T. Jacobsen, “Impedance Modeling of Solid Oxide Fuel Cell Cathodes,” *ECS Trans*, vol. 28, no. 11, pp. 17–38, Dec. 2010, doi: 10.1149/1.3495830.

[11] S. B. Adler, J. A. Lane, and B. C. H Steele, “Electrode Kinetics of Porous Mixed-Conducting Oxygen Electrodes,” *J Electrochem Soc*, vol. 143, no. 11, p. 363, 1996.

[12] A. Haffelin, J. Joos, M. Ender, A. Weber, and E. Ivers-Tiffee, “Transient 3D FEM Impedance-Model for Mixed Conducting Cathodes,” *ECS Trans*, vol. 45, no. 1, pp. 313–325, Apr. 2012, doi: 10.1149/1.3701321.

[13] J. Joos, “Microstructural Characterisation, Modelling and Simulation of Solid Oxide Fuel Cell Cathodes,” PhD thesis, Karlsruher Institut für Technologie, Karlsruher, 2015.

[14] T. A. Schmauss and S. A. Barnett, “Atomic layer deposition for surface area determination of solid oxide electrodes,” *J Mater Chem A Mater*, vol. 11, no. 7, pp. 3695–3702, 2023, doi: 10.1039/D2TA09060K.

[15] J. Song, D. Ning, B. Boukamp, J. M. Bassat, and H. J. M. Bouwmeester, “Structure, electrical conductivity and oxygen transport properties of Ruddlesden–Popper phases Lnn+1NinO3n+1 (Ln = La, Pr and Nd; n = 1, 2 and 3),” *J Mater Chem A Mater*, vol. 8, no. 42, pp. 22206–22221, Nov. 2020, doi: 10.1039/D0TA06731H.

[16] A. P. Tarutin, J. G. Lyagaeva, D. A. Medvedev, L. Bi, and A. A. Yaremchenko, “Recent advances in layered $Ln_2NiO_{4+\delta}$ nickelates: fundamentals and prospects of their applications in protonic ceramic fuel and electrolysis cells,” *J Mater Chem A Mater*, vol. 9, no. 1, pp. 154–195, 2021, doi: 10.1039/D0TA08132A.

[17] N. Hildenbrand, P. Nammensma, D. H. A. Blank, H. J. M. Bouwmeester, and B. A. Boukamp, “Influence of configuration and microstructure on performance of La 2NiO4+δ intermediate-

temperature solid oxide fuel cells cathodes," *J Power Sources*, vol. 238, pp. 442–453, 2013, doi: 10.1016/j.jpowsour.2013.03.192.

[18] M. A. Morales-Zapata, A. Larrea, and M. A. Laguna-Bercero, "Lanthanide nickelates for their application on Solid Oxide Cells," *Electrochim Acta*, vol. 444, Mar. 2023, doi: 10.1016/j.electacta.2023.141970.

[19] R. K. Sharma, M. Burriel, L. Dessemond, J. M. Bassat, and E. Djurado, "Design of interfaces in efficient Ln2NiO4+δ (Ln = La, Pr) cathodes for SOFC applications," *J Mater Chem A Mater*, vol. 4, no. 32, pp. 12451–12462, Aug. 2016, doi: 10.1039/C6TA04845E.

[20] A. Stangl *et al.*, "Tailored nano-columnar La2NiO4 cathodes for improved electrode performance," *J Mater Chem A Mater*, vol. 10, pp. 2528–2540, 2022, doi: 10.1039/D1TA09110G.

[21] T. Carraro, J. Joos, B. Rüger, A. Weber, and E. Ivers-Tiffée, "3D Finite Element Model for Reconstructed Mixed-Conducting Cathodes: I. Performance Quantification," *Electrochim Acta*, vol. 77, pp. 315–323, Aug. 2012, doi: 10.1016/j.electacta.2012.04.109.

[22] J. Joos, T. Carraro, M. Ender, B. Rüger, A. Weber, and E. Ivers-Tiffée, "Detailed Microstructure Analysis and 3D Simulations of Porous Electrodes," *ECS Trans*, vol. 35, no. 1, pp. 2357–2368, Dec. 2011, doi: 10.1149/1.3570232.

[23] J. Laurencin *et al.*, "Reactive Mechanisms of LSCF Single-Phase and LSCF-CGO Composite Electrodes Operated in Anodic and Cathodic Polarisations," *Electrochim Acta*, vol. 174, pp. 1299–1316, Jul. 2015, doi: 10.1016/j.electacta.2015.06.080.

[24] L. Ma, P. Priya, and N. R. Aluru, "A Multiscale Model for Electrochemical Reactions in LSCF Based Solid Oxide Cells," *J Electrochem Soc*, vol. 165, no. 14, pp. F1232–F1241, 2018, doi: 10.1149/2.0921814jes.

[25] M. Hubert *et al.*, “Role of microstructure on electrode operating mechanisms for mixed ionic electronic conductors: From synchrotron-based 3D reconstruction to electrochemical modeling,” *Solid State Ion*, vol. 294, pp. 90–107, Oct. 2016, doi: 10.1016/j.ssi.2016.07.001.

[26] G. Sdanghi *et al.*, “Reaction Mechanisms of $La_2NiO_{4+\delta}$ Oxygen Electrodes Operated in Electrolysis and Fuel Cell Mode,” *J Electrochem Soc*, vol. 169, no. 3, p. 034518, Mar. 2022, doi: 10.1149/1945-7111/ac58c3.

[27] R. Suwanwarangkul, E. Croiset, M. W. Fowler, P. L. Douglas, E. Entchev, and M. A. Douglas, “Performance comparison of Fick’s, dusty-gas and Stefan-Maxwell models to predict the concentration overpotential of a SOFC anode,” *J Power Sources*, vol. 122, no. 1, pp. 9–18, Jul. 2003, doi: 10.1016/S0378-7753(02)00724-3.

[28] E. L. Cussler, “Diffusion: Mass Transfer in Fluid Systems,” Cambridge, 2009. [Online]. Available: www.cambridge.org/cussler.

[29] J.-C. Grenier *et al.*, “ Lanthanide Nickelates Ln 2 NiO 4+ δ (Ln = La, Pr or Nd): Promising Cathode Materials For Metal Supported Cells ,” *ECS Trans*, vol. 57, no. 1, pp. 1771–1779, Oct. 2013, doi: 10.1149/05701.1771ecst.

[30] A. Flura *et al.*, “ Application of the Adler-Lane-Steele Model to Porous La 2 NiO 4+ δ SOFC Cathode: Influence of Interfaces with Gadolinia Doped Ceria ,” *J Electrochem Soc*, vol. 163, no. 6, pp. F523–F532, Mar. 2016, doi: 10.1149/2.0891606JES/XML.

[31] J. Fleig, “On the width of the electrochemically active region in mixed conducting solid oxide fuel cell cathodes,” *Journal of Power Sources* , vol. 105, pp. 228–238, 2002.

[32] J. Deseure, Y. Bultel, L. Dessemond, and E. Siebert, “Theoretical optimisation of a SOFC composite cathode,” *Electrochim Acta*, vol. 50, no. 10, pp. 2037–2046, Mar. 2005, doi: 10.1016/J.ELECTACTA.2004.09.012.

[33] J. Fleig and J. Maier, “The polarization of mixed conducting SOFC cathodes: Effects of surface reaction coefficient, ionic conductivity and geometry,” *J Eur Ceram Soc*, vol. 24, no. 6, pp. 1343–1347, 2004, doi: 10.1016/S0955-2219(03)00561-2.

[34] Özden Çelikbilek *et al.*, “Rational design of hierarchically nanostructured electrodes for solid oxide fuel cells,” *J Power Sources*, vol. 333, pp. 72–82, Nov. 2016, doi: 10.1016/j.jpowsour.2016.09.156.

[35] Z. Yan, A. He, S. Hara, and N. Shikazono, “Modeling of solid oxide fuel cell (SOFC) electrodes from fabrication to operation: Correlations between microstructures and electrochemical performances,” *Energy Convers Manag*, vol. 190, pp. 1–13, Jun. 2019, doi: 10.1016/j.enconman.2019.04.002.

[36] C. R. Kreller *et al.*, “Modeling SOFC cathodes based on 3-D representations of electrode microstructure,” *ECS Trans*, vol. 35, no. 1, pp. 815–822, 2011, doi: 10.1149/1.3570062.

[37] J. A. Taillon, C. Pellegrinelli, Y. L. Huang, E. D. Wachsman, and L. G. Salamanca-Riba, “Improving microstructural quantification in FIB/SEM nanotomography,” *Ultramicroscopy*, vol. 184, no. Pt A, pp. 24–38, Jan. 2018, doi: 10.1016/J.ULTRAMIC.2017.07.017.

[38] M. Neumann, J. Staněk, O. M. Pecho, L. Holzer, V. Beneš, and V. Schmidt, “Stochastic 3D modeling of complex three-phase microstructures in SOFC-electrodes with completely connected phases,” *Comput Mater Sci*, vol. 118, pp. 353–364, Jun. 2016, doi: 10.1016/j.commatsci.2016.03.013.

[39] H. Moussaoui *et al.*, “Stochastic geometrical modeling of solid oxide cells electrodes validated on 3D reconstructions,” *Comput Mater Sci*, vol. 143, pp. 262–276, Feb. 2018, doi: 10.1016/J.COMMATSCI.2017.11.015.

[40] J. Villanova *et al.*, “Multi-scale 3D imaging of absorbing porous materials for solid oxide fuel cells.,” *J Mater Sci*, vol. 49, no. 16, pp. 5626–5634, 2014, doi: 10.1007/S10853-014-8275-3.

[41] G. T. Kim, S. Wang, A. J. Jacobson, Z. Yuan, and C. Chen, “Impedance studies of dense polycrystalline thin films of La 2NiO4+δ,” *J Mater Chem*, vol. 17, no. 13, pp. 1316–1320, 2007, doi: 10.1039/b616101d.

[42] J. Ascolani-Yael *et al.*, “The oxygen reduction reaction in solid oxide fuel cells: from kinetic parameters measurements to electrode design,” *Journal of Physics: Energy*, vol. 2, no. 4, p. 042004, Oct. 2020, doi: 10.1088/2515-7655/abb4ec.

[43] A. Egger and W. Sitte, “Enhanced oxygen surface exchange of La2NiO4+δ by means of a thin surface layer of silver,” *Solid State Ion*, vol. 258, pp. 30–37, May 2014, doi: 10.1016/j.ssi.2014.01.038.

[44] D. Lee *et al.*, “Strain influence on the oxygen electrocatalysis of the (100)-oriented epitaxial La2NiO4+δ thin films at elevated temperatures,” *Journal of Physical Chemistry C*, vol. 117, no. 37, pp. 18789–18795, Sep. 2013, doi: 10.1021/jp404121p.

[45] R. Sayers and S. J. Skinner, “Evidence for the catalytic oxidation of La_2NiO_{4+} δ,” *J. Mater. Chem.*, vol. 21, no. 2, pp. 414–419, 2011, doi: 10.1039/C0JM02419H.

[46] S. Skinner and J. A. Kilner, “Oxygen diffusion and surface exchange in La2−xSrxNiO4+δ,” *Solid State Ion*, vol. 135, no. 1–4, pp. 709–712, Nov. 2000, doi: 10.1016/S0167-2738(00)00388-X.

[47] J. Kilner and C. K. M. Shaw, “Mass transport in La2Ni1−xCoxO4+δ oxides with the K2NiF4 structure,” *Solid State Ion*, vol. 154–155, pp. 523–527, Dec. 2002, doi: 10.1016/S0167-2738(02)00506-4.

[48] E. Boehm, J. M. Bassat, M. C. Steil, P. Dordor, F. Mauvy, and J. C. Grenier, “Oxygen transport properties of La2Ni1-xCuxO4+δ mixed conducting oxides,” *Solid State Sci*, vol. 5, no. 7, pp. 973–981, Jul. 2003, doi: 10.1016/S1293-2558(03)00091-8.

[49] M. Burriel, G. Garcia, M. D. Rossell, A. Figueras, G. Van Tendeloo, and J. Santiso, “Enhanced high-temperature electronic transport properties in nanostructured epitaxial thin films of the Lan+1NinO3n+1 Ruddlesden-Popper series (n = 1, 2, 3, ∞),” *Chemistry of Materials*, vol. 19, no. 16, pp. 4056–4062, Aug. 2007, doi: 10.1021/cm070804e.

[50] Z. Li and R. Haugsrud, “Effects of surface coatings on the determination of Dchem and kchem in La2NiO4+δ by conductivity relaxation,” *Solid State Ion*, vol. 206, pp. 67–71, Jan. 2012, doi: 10.1016/J.SSI.2011.11.011.

[51] W. Li, B. Guan, X. Zhang, J. Yan, Y. Zhou, and X. Liu, “New mechanistic insight into the oxygen reduction reaction on Ruddlesden–Popper cathodes for intermediate-temperature solid oxide fuel cells,” *Physical Chemistry Chemical Physics*, vol. 18, no. 12, pp. 8502–8511, Mar. 2016, doi: 10.1039/C6CP00056H.

[52] T. Ishihara, “Development of new fast oxide ion conductor and application for intermediate temperature Solid Oxide Fuel Cells,” *Bull Chem Soc Jpn*, vol. 79, no. 8, pp. 1155–1166, 2006, doi: 10.1246/BCSJ.79.1155.

[53] V. Vibhu, A. Rougier, C. Nicollet, A. Flura, J.-C. Grenier, and J.-M. Bassat, “La2-xPrxNiO4+δ as suitable cathodes for metal supported SOFCs La 2-x Pr x NiO 4+δ as suitable cathodes for Metal Supported SOFCs,” *Solid State Ion*, vol. 278, pp. 32–37, 2015, doi: 10.1016/j.ssi.2015.05.005ï.

[54] C. Ahamer, A. K. Opitz, G. M. Rupp, and J. Fleig, “Revisiting the Temperature Dependent Ionic Conductivity of Yttria Stabilized Zirconia (YSZ),” *J Electrochem Soc*, vol. 164, no. 7, pp. F790–F803, 2017, doi: 10.1149/2.0641707jes.

[55] B. A. Boukamp, “Distribution (function) of relaxation times, successor to complex nonlinear least squares analysis of electrochemical impedance spectroscopy?,” *Journal of Physics: Energy*, vol. 2, no. 4, p. 042001, Oct. 2020, doi: 10.1088/2515-7655/aba9e0.

[56] S. Dierickx, A. Weber, and E. Ivers-Tiffée, “How the distribution of relaxation times enhances complex equivalent circuit models for fuel cells,” *Electrochim Acta*, vol. 355, p. 136764, 2020, doi: 10.1016/j.electacta.2020.136764.

[57] D. Pérez-Coll, A. Aguadero, M. J. Escudero, and L. Daza, “Effect of DC current polarization on the electrochemical behaviour of La2NiO4+δ and La3Ni2O7+δ-based systems,” *J Power Sources*, vol. 192, no. 1, pp. 2–13, Jul. 2009, doi: 10.1016/j.jpowsour.2008.10.073.

[58] G. Sdanghi *et al.*, “Reaction Mechanisms of $La_2NiO_{4+\delta}$ Oxygen Electrodes Operated in Electrolysis and Fuel Cell Mode,” *J Electrochem Soc*, vol. 169, no. 3, p. 034518, Mar. 2022, doi: 10.1149/1945-7111/ac58c3.

[59] W. G. Bessler, S. Gewies, and M. Vogler, “A new framework for physically based modeling of solid oxide fuel cells,” *Electrochim Acta*, vol. 53, no. 4, pp. 1782–1800, Dec. 2007, doi: 10.1016/j.electacta.2007.08.030.

[60] F. Monaco *et al.*, “Experimental validation of a La0.6Sr0.4Co0.2Fe0.8O3-δ electrode model operated in electrolysis mode: Understanding the reaction pathway under anodic polarization,” *Solid State Ion*, vol. 319, pp. 234–246, Jun. 2018, doi: 10.1016/j.ssi.2018.02.012.